

Catalytic Properties of Pt Cluster-Decorated CeO₂ Nanostructures

Lin Feng^{1,2}, Dat Tien Hoang¹, Chia-Kuang Tsung^{1,3}, Wenyu Huang¹, Sylvia Hsiao-Yun Lo¹, Jennifer B. Wood¹, Hungta Wang¹, Jinyao Tang¹, and Peidong Yang¹ (✉)

¹ Department of Chemistry, University of California, Berkeley, California 94720, USA

² Department of Chemistry, Tsinghua University, Beijing 100084, China

³ Department of Chemistry, Merkert Chemistry Center, Boston College, 2609 Beacon Street, Chestnut Hill, Massachusetts 02467, USA

Received: 24 August 2010 / Revised: 9 September 2010 / Accepted: 9 September 2010

© The Author(s) 2010. This article is published with open access at Springerlink.com

ABSTRACT

Uniform clusters of Pt have been deposited on the surface of capping-agent-free CeO₂ nanooctahedra and nanorods using electron beam (e-beam) evaporation. The coverage of the Pt nanocluster layer can be controlled by adjusting the e-beam evaporation time. The resulting e-beam evaporated Pt nanocluster layers on the CeO₂ surfaces have a clean surface and clean interface between Pt and CeO₂. Different growth behaviors of Pt on the two types of CeO₂ nanocrystals were observed, with epitaxial growth of Pt on CeO₂ nanooctahedra and random growth of Pt on CeO₂ nanorods. The structures of the Pt clusters on the two different types of CeO₂ nanocrystals have been studied and compared by using them as catalysts for model reactions. The results of hydrogenation reactions clearly showed the clean and similar chemical surface of the Pt clusters in both catalysts. The support-dependent activity of these catalysts was demonstrated by CO oxidation. The Pt/CeO₂ nanorods showed much higher activity compared with Pt/CeO₂ nanooctahedra because of the higher concentration of oxygen vacancies in the CeO₂ nanorods. The structure-dependent selectivity of dehydrogenation reactions indicates that the structures of the Pt on CeO₂ nanorods and nanooctahedra are different. These differences arise because the metal deposition behaviors are modulated by the strong metal–metal oxide interactions.

KEYWORDS

Nanocrystals, nanoclusters, interface, catalysis

1. Introduction

Metal nanoparticles and metal oxide supports are two major components of most heterogeneous catalysts [1–4]. It is well known that catalytic activity and selectivity are highly dependent on the type of metal oxide support used [5–7], and catalysis can be modulated by using different metal oxide supports [8]. A great deal of research has been devoted to understanding the interaction between metals and

different metal oxide supports in order to design better catalysts [9–12]. Recently, cerium oxide (CeO₂) has become a very attractive candidate as a metal oxide support [13–15]. CeO₂ has extensively documented oxygen storage capacity (OSC) [16–18] and results in strong metal–metal oxide interactions [19]. Due to these unique properties, metal/CeO₂ catalysts show great activity for reactions such as hydrogenation, the water gas shift, and CO and hydrocarbon oxidation [20–22]. Most previous studies have focused on traditional

Address correspondence to p_yang@berkeley.edu



supported metal catalysts, which are prepared by depositing metal clusters on the surface of micron-size CeO₂ supports. However, in these studies the size, shape, and crystal structure of the CeO₂ supports were not controlled at the nanoscale [23–25]. Less attention has been paid to the effects of the nanostructure of CeO₂ supports. Flytzani-Stephanopoulos et al. reported one of the few catalytic studies using different nanostructured CeO₂ materials, employing them as a support to deposit gold clusters [26]. The resulting Au/CeO₂ catalysts showed a strong support-shape effect in the water gas shift reaction. Further studies of the deposition of different metal clusters on nanostructured CeO₂ are merited because of two consequences of the strong metal–metal oxide interaction: The interaction potentially changes the intrinsic properties of the metal and metal oxide, and moreover, is strong enough to affect metal growth behavior on deposition. Further study of deposition methods would also be useful in understanding this phenomenon.

Electron beam (e-beam) evaporation is a frequently used method for the preparation of overgrowth thin films or thin cluster layers on substrates. It is popular because of its conceptual and experimental simplicity; the source material is transformed into its gaseous state, which is then condensed on the substrate. The clean surface and chemical purity of the resulting evaporated cluster layer make it ideal for the synthesis of model catalysts. Herein, we describe the use of the e-beam evaporation method and shape controlled metal oxide nanostructures to synthesize model catalysts. In this instance, shape-specific CeO₂ nanocrystals were first synthesized and subsequently decorated with a thin Pt cluster layer. The as-synthesized CeO₂ nanocrystals have no organic capping. The structure of the composite nanomaterials was analyzed by electron microscopy. The nanosupport-dependent catalytic behaviors were demonstrated by model hydrogenation, dehydrogenation, and oxidation reactions. The information gained from this study will lead to a better understanding of the interactions between metals and metal oxides.

2. Methods

2.1 Characterization methods and instrumentation

Powder X-ray diffraction (XRD) patterns were recorded

with a GADDS Hi-Star D8 diffractometer (Bruker) using Co K α radiation ($\lambda = 1.790 \text{ \AA}$). XRD samples were prepared by depositing the precipitated samples on a silicon plate. The sizes and morphologies of the as-obtained nanocrystals were examined with a FEI Tecnai G2 S-Twin transmission electron microscope at an accelerating voltage of 200 kV and a field emission scanning electron microscope (FESEM, JEOL6430) with an operating voltage of 5 kV. The samples were prepared by casting the dilute colloidal solution onto carbon-coated copper transmission electron microscopy (TEM) grids and silicon wafers, respectively. X-ray photoelectron spectroscopy (XPS) experiments were performed on a Perkin–Elmer PHI 5300 XPS spectrometer with a position-sensitive detector and a hemispherical energy analyzer in an ion-pumped chamber (evacuated to 2×10^{-9} Torr). The Al K α ($h\nu = 1486.6 \text{ eV}$) X-ray source was operated at 300 W with 15 kV acceleration voltage. Binding energies (BE) were calibrated by setting the measured BE of C 1s to 285 eV.

2.2 Synthesis of CeO₂ nanorods and nanooctahedra

The uniform organic-capping-free CeO₂ nanostructures were synthesized in two morphologies, rod-like and octahedral, by using a hydrothermal process [27]. Ce(NO₃)₃·6H₂O was used as the cerium source. No organic surfactant or template was introduced in the synthesis. For CeO₂ nanooctahedra, 434.3 mg of Ce(NO₃)₃·6H₂O and 1.6 mg of Na₃PO₄ were mixed in 40 mL of D.I. H₂O and sonicated for 30 min. The mixed solution with of pH 4 was then transferred into the Teflon-liner of a hydrothermal autoclave. The autoclave was heated to 170 °C for 12 h. The as-synthesized CeO₂ nanooctahedra were collected and cleaned by centrifugation at 10,000 r/min for 5 min and re-dispersed twice in ethanol. The supernatant was discarded and the precipitated product was then calcined at 400 °C for 4 h. The CeO₂ nanorods were synthesized by adjusting the pH value of the precursor solution from 4 to 2 with dilute hydrochloric acid solution and employing the same hydrothermal treatment. For the synthesis of the CeO₂ nanorods, the pH value is very crucial and needs to be very precise.

2.3 E-beam evaporation of Pt

A homogeneous thick layer of CeO₂ nanostructures

was drop casted on a 1.8×0.9 cm silicon wafer. After Ar plasma treatment for few seconds, a low density Pt nanocluster layer was deposited by an e-beam evaporator with a background pressure of $\sim 2 \times 10^{-6}$ Torr. The Pt evaporation rate and deposition thickness were monitored by a crystal monitor. The evaporation rate is controlled by the electron beam current and was fixed at 0.01 nm/s. Different amounts of Pt were deposited by varying the evaporation time.

2.4 Ethylene hydrogenation and cyclohexene hydrogenation/dehydrogenation

Catalytic activities of CeO₂ nanooctahedra and nanorods with the same amount of deposited Pt were measured and compared. For catalytic studies, samples were loaded into glass reactors. Temperature was controlled by a proportional–integral–derivative (PID) controller (Watlow 96) and a type-K thermocouple. Gases were all ultrahigh-purity (UHP) from Praxair. Gas flows were regulated using calibrated mass flow controllers. Before the reaction, samples were reduced in 50 mL·min⁻¹ of 76 Torr of H₂ with a He balance for 1 h at 100 °C. For ethylene hydrogenation, the gas mixture was composed of 10 Torr of ethylene and 100 Torr of H₂ with a balance of He. For cyclohexene hydrogenation/dehydrogenation, the feed was 10 Torr of C₆H₁₀ (Sigma–Aldrich) and 200 Torr of H₂ with a balance of He. The desired partial pressure of C₆H₁₀ was achieved by bubbling He through C₆H₁₀ and assuming saturation. All lines before and after the quartz U-tube reactor were heated to 393 K to prevent condensation of organic compounds.

2.5 CO oxidation

The CO oxidation reaction was also used to evaluate the catalytic properties of Pt/CeO₂ nanooctahedra and nanorods. CO oxidation reactions were carried out in a laboratory scale reactor with gas recirculation. The reaction temperature was between 170 and 230 °C. Samples were loaded into quartz reactors and the reaction temperature was recorded by a type-K thermocouple placed near the sample. Prior to the reaction, the reactor was filled with 40 Torr of CO, 100 Torr of O₂, and 620 Torr of He. Gas composition was analyzed with a HP 5890 Series II gas chromatograph

equipped with a thermal conductivity (TCD) detector. Turnover frequency (TOF) was calculated by extrapolating the conversion data to the initial time. The numbers of available Pt active sites on the catalysts were calculated from the TEM and ethylene hydrogenation reaction.

3. Results and discussion

3.1 CeO₂ nanorods and nanooctahedra without organic capping agents

The structures of as-synthesized CeO₂ nanooctahedra and nanorods were confirmed by Scanning electron microscope (SEM) and TEM (Fig. 1). Even without organic capping agents, CeO₂ nanostructures were well-dispersed and no aggregation of nanocrystals was observed under SEM imaging. Furthermore, well-defined morphologies can easily be obtained by simply adjusting the pH value of the precursor. The TEM images show that both CeO₂ octahedra and rods have high uniformity and well-defined morphologies (Figs. 1(c) and 1(d)). The edge length of the octahedra is ~ 100 nm. The widths of the CeO₂ nanorods are ~ 20 nm and the lengths are around several hundred nanometers. The crystal structures of the CeO₂ nanostructures were confirmed by XRD (Fig. 2). The diffraction peaks of both octahedra and rods can be indexed to cubic phase CeO₂ (JCPDF 43-1002). The organic-capping-free surface and good dispersion of the CeO₂ nanostructures are the two most critical factors for the subsequent step involving Pt deposition on the surface of CeO₂ via e-beam evaporation.

The detailed shape and crystal facets of the CeO₂ nanostructures were studied by high-resolution transmission electron microscopy (HRTEM). The HRTEM images of octahedral CeO₂ show lattice planes with d-spacing of 0.32 nm corresponding to the (111) planes of cubic CeO₂ (Figs. 3(a) and 3(b)). This suggests that the octahedra were mainly enclosed by (111) facets, which have the highest surface density of atoms and the lowest surface energy for a face-centered cubic structure. Truncated apexes of the CeO₂ octahedra were observed on some of the HRTEM images. The exposed facets of the truncated apexes are (200). Figures 3(c) and 3(d) show typical HRTEM images of



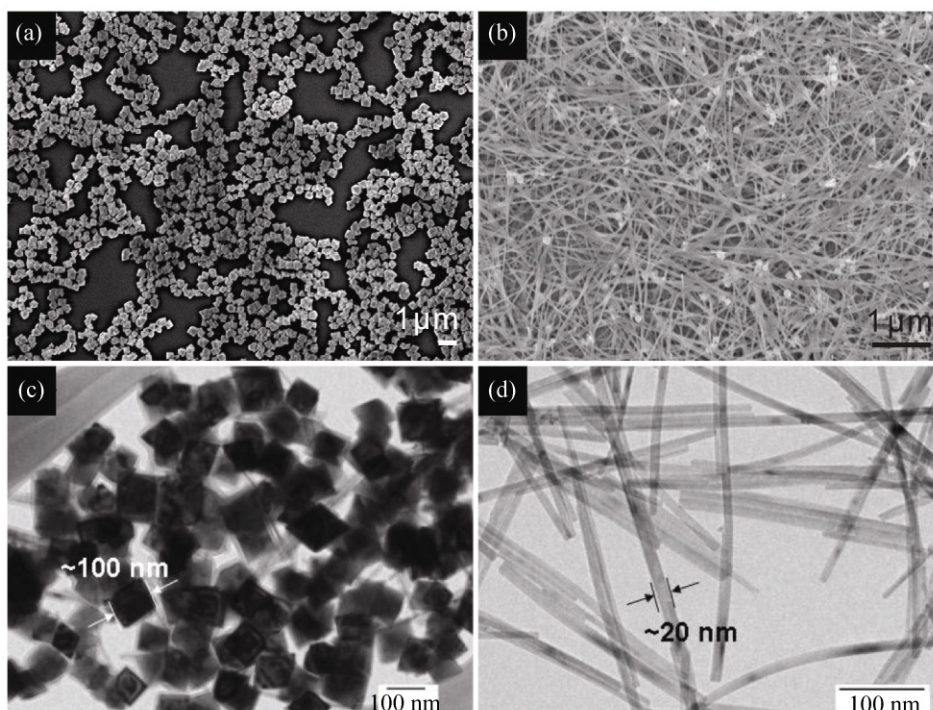


Figure 1 SEM and TEM images of (a) and (c) CeO₂ nanooctahedra (b) and (d) CeO₂ nanorods

the CeO₂ nanorods. The clear lattice images indicate the good crystallinity and single crystalline nature of the CeO₂ nanorods. The interplanar spacings in the HRTEM images suggest that the predominant facets of the CeO₂ nanorods are (200) and (110), rather than the (111) facets found for the nanooctahedra. The nanorods are characterized by rough edges, in contrast to the smooth edges of the nanooctahedra; this represents an additional important difference between the surfaces of the two materials.

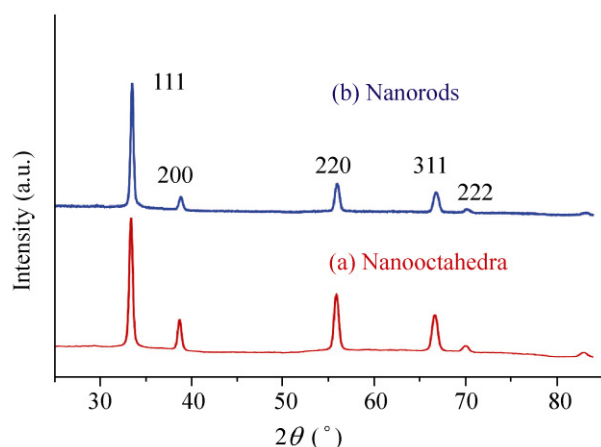


Figure 2 XRD patterns of (a) CeO₂ nanooctahedra. (b) CeO₂ nanorods

As shown in Fig. 4, Ce (3d) XPS of both rod and octahedron-shaped CeO₂ shows characteristic main and satellite peaks due to Ce⁴⁺ and Ce³⁺ ions. Due to the complexity of the XPS, we followed the deconvolution procedure described by Schierbaum [28] and Kotani [29]. The XPS of Ce³⁺ (3d_{5/2}) shows two binding energy peaks at 880 and 885 eV (satellite peak). For Ce⁴⁺ (3d_{5/2}), the XPS shows three binding energy peaks at 882.6, 888.4 (satellite peak), and 898.2 eV (satellite peak). The other five peaks at higher binding energy correspond to the 3d_{3/2} states of Ce³⁺ and Ce⁴⁺ ions with 2/3 of the intensity of the corresponding 3d_{5/2} peaks. All peak positions were fixed for the two spectra in order to comparing their relative intensity. It is very clear that the CeO₂ rods contain more Ce³⁺ compared to the octahedral CeO₂. From the deconvoluted peak area, Ce³⁺ ions account for 59.8% of cerium on the surface of CeO₂ rods, while only 28% of cerium on the CeO₂ octahedra is in the Ce³⁺ state.

3.2 Deposition of Pt nanoclusters on CeO₂ nanostructure surface

Silicon wafers and TEM grids with CeO₂ nanorods and nanooctahedra layers were used as the substrates

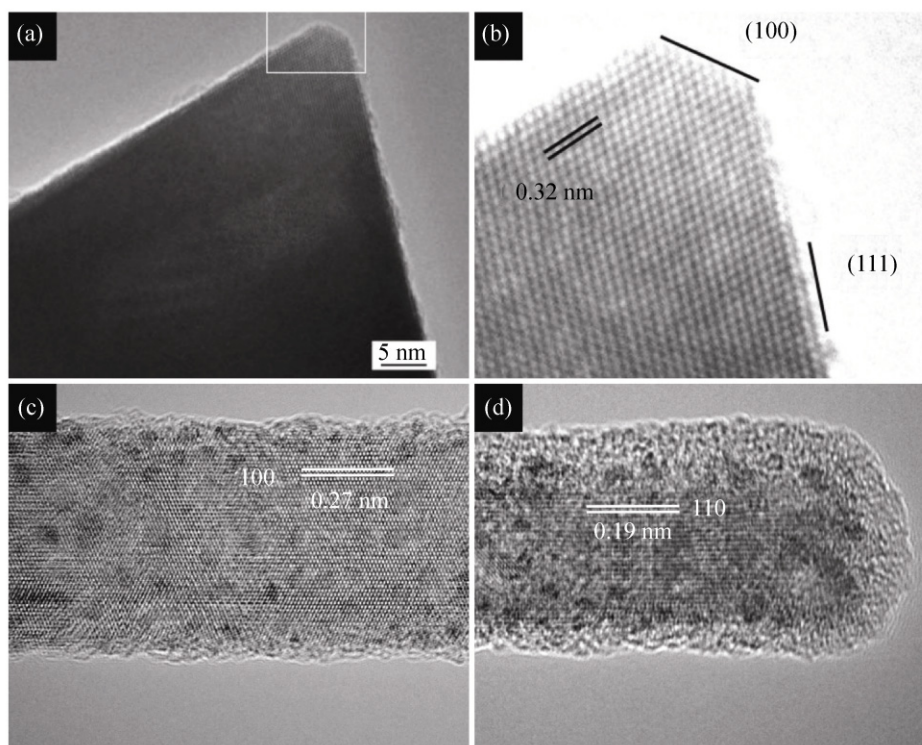


Figure 3 (a) HRTEM image of a CeO₂ nanooctahedron. (b) Shows a magnified view of the selected area of (a). (c) and (d) HRTEM images of CeO₂ nanorods

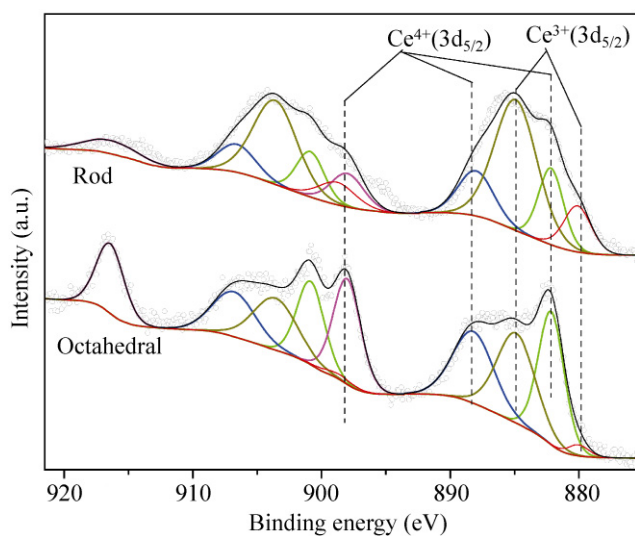


Figure 4 Ce (3d) XPS spectra of CeO₂ nanorods and CeO₂ nanooctahedra

for e-beam Pt evaporation for the purpose of catalysis studies and TEM analyses, respectively. The Pt evaporation rate and deposition amount were monitored by a crystal monitor. The evaporation rate was controlled by the e-beam current and was fixed at 0.01 nm/s.

The amount of Pt deposited was controlled by varying the evaporation time. Figures 5(a) and 6(a) show TEM images of Pt cluster layers on CeO₂ nanooctahedra and nanorods, respectively, after an evaporation time of 20 seconds. Pt nanoclusters with a uniform diameter of about 1 nm were distributed evenly on both CeO₂ octahedra and rods. Figures 5(b), 5(c), and 5(d) show HRTEM images of an individual Pt/CeO₂ nanooctahedron. Figure 5(d) and the inset of Fig. 5(b) show magnified views of the selected areas in Figs. 5(c) and 5(b), respectively. These HRTEM images clearly show that most Pt nanoclusters are oriented in the [111] direction on the surface of the CeO₂ nanooctahedron, which is the (111) facet of CeO₂. The magnified views show the great structural homogeneity and high degree of alignment of the (111) zone axis of the Pt nanoclusters. This suggests an epitaxial growth of Pt on the surface of the CeO₂ octahedra. The HRTEM image of CeO₂ nanorods after Pt deposition for 20 seconds is shown in Fig. 6(b). The HRTEM image of Pt deposition on CeO₂ indicates that Pt nanoclusters were oriented in the [111] direction on

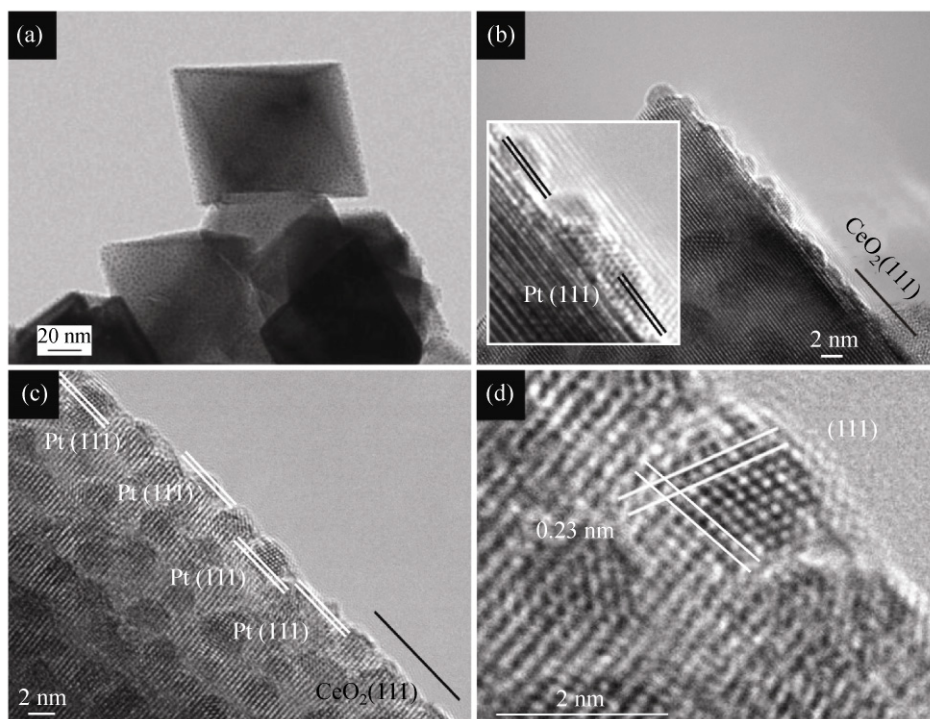


Figure 5 (a) TEM image of CeO₂ nanooctahedra decorated with a Pt nanocluster layer. (b, c) HRTEM images of CeO₂ nanooctahedra decorated with a Pt layer. (d) and the inset in (b) show magnified views of the selected areas in (c) and (b), respectively

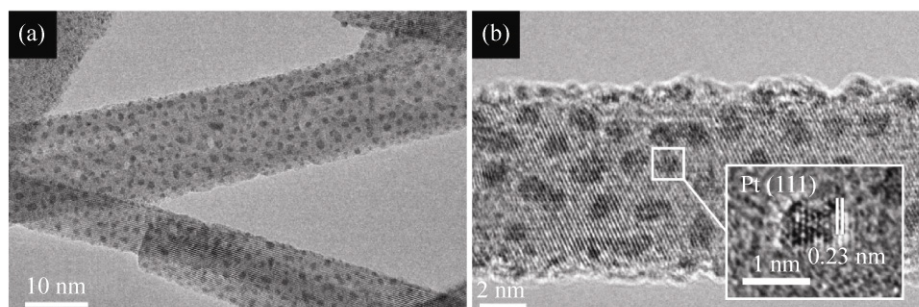


Figure 6 (a) TEM image of CeO₂ nanorods coated with a Pt nanocluster layer and (b) HRTEM images of CeO₂ nanorods coated with a Pt layer. The inset in (b) shows a magnified view of the selected area

the surface of the CeO₂ nanorods. The nanoclusters were slightly smaller than the Pt nanoclusters on found on the nanooctahedra. In order to further investigate the growth of Pt on the CeO₂ rods, longer evaporation times were also employed. HRTEM images (Fig. 7) indicate that most of the resulting 3 nm Pt nanoclusters were also oriented in the [111] direction on the surface of the CeO₂ nanorods. The magnified views indicate the high degree of crystallinity of the Pt nanoclusters but no lattice alignment was observed. It is worth mentioning that the coverage of Pt for the samples with 3 nm Pt was very high. About 40–50% of

the CeO₂ surface that was exposed to the evaporation was covered by Pt. However, the coverage of the opposite sides of the nanorods is low due to the shadow effect.

In the case of the nanooctahedron, it is enclosed solely by (111) facets. The relatively smooth (111) facets of the octahedra are indicated by the clear and sharp edges of the octahedra in the TEM images. These large and smooth (111) facets on the octahedra provide ideal substrates for Pt deposition and contribute to the epitaxial growth of Pt nanoclusters. In contrast, CeO₂ nanorods have different exposed surface planes

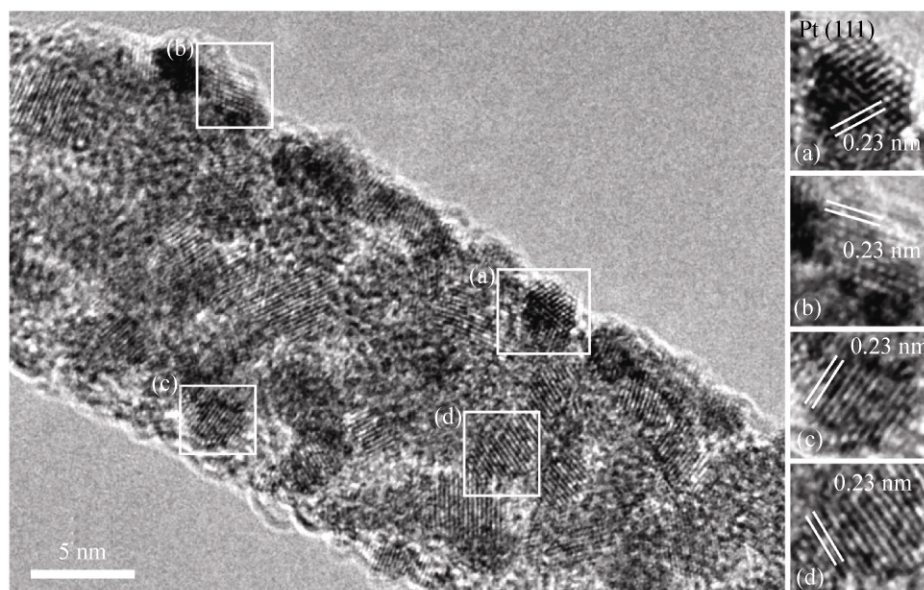


Figure 7 HRTEM image of a CeO₂ nanorod with 3 nm thick Pt deposition

and different Pt cluster growth is observed. Our observations clearly indicate that the structure of the CeO₂ nanocrystals plays an important role in Pt deposition. Different structures of the CeO₂ support result in different growth behaviors of Pt. The different growth behaviors affect the size, structure, and coverage of Pt on CeO₂. All these parameters change the stability, activity, and selectivity of the Pt on CeO₂ catalysts.

3.3 Catalysis

The activities and selectivities of Pt/CeO₂ catalysts for model hydrogenation and oxidation reactions were measured and compared. In order to determine the turnover frequency (TOF), the number of active sites in the Pt catalysts has to be determined first. The number of available Pt sites for reactions is generally determined from H₂ or CO chemisorption measurements [30, 31]. However, for our model catalysts this technique is very challenging, due to the limited amount of metal deposited. It has been demonstrated that ethylene hydrogenation can be used as a chemical probe for estimating the number of available metallic Pt active sites in a catalyst [32]. Ethylene hydrogenation is a classic example of a structure insensitive reaction. The intrinsic catalytic activity is not a function of the Pt surface for this catalytic reaction, which makes it

an ideal way to determine the number of available Pt sites. The number of available Pt sites for different Pt/CeO₂ catalysts were calculated and determined by using the TOF of ethylene hydrogenation at 35, 40, 45, 50, and 55 °C, with single crystal and standard Pt catalysts as references. The results are shown in Table 1.

CO oxidation was used as a model reaction to characterize the catalytic properties of Pt/CeO₂ nano-octahedra and nanorods. CeO₂ is an important component in automobile exhaust converters, which is due to its exceptional OSC [33]. During engine operation, CeO₂ adsorbs oxygen from the exhaust under lean conditions (high air-to-fuel ratio) and releases oxygen into the exhaust under rich conditions (low air-to-fuel ratio). CeO₂ undergoes reversible Ce⁴⁺/Ce³⁺ redox reactions when it adsorbs or releases oxygen. The superior OSC of CeO₂ maintains the air-to-fuel ratio in the exhaust; this is crucial for ensuring high efficiency of the three-way catalysts in the automobile exhaust converter [34]. The OSC also greatly alters the mechanism of the CO oxidation reaction catalyzed by precious metals supported on CeO₂. In a Pt catalyzed CO oxidation reaction, the oxygen reaction order as well as the reaction activation energy is much lower when CeO₂ is used as the support compared to γ -Al₂O₃ [35]. This indicates that the

Table 1 Catalytic behavior over the Pt/CeO₂ nanostructure catalysts

Catalyst	Available Pt sites (atom) ^a	E_a of ethylene hydrogenation (kcal/mol) ^b	TOF of CO oxidation at 200 °C (s ⁻¹) ^{c, e}	E_a of CO oxidation (kcal/mol) ^{e, f}	TOF of cyclohexene hydrogenation at 120 °C (s ⁻¹) ^{d, e}	E_a of cyclohexene hydrogenation (kcal/mol) ^{e, f}	TOF of cyclohexene dehydrogenation at 150 °C (s ⁻¹) ^{d, e}	E_a of cyclohexene dehydrogenation (kcal/mol) ^{e, f}
Pt/CeO ₂ nanooctahedra	6.41×10^{14}	8.87	0.18	34.70	10.23	10.98	4.59	20.13
Pt/CeO nanorods	8.22×10^{14}	7.94	3.10	24.30	10.00	8.52	9.72	25.47

^a The number of available Pt sites was determined by TOF of ethylene hydrogenation.

^b Standard conditions were 10 Torr of ethylene and 100 Torr of H₂ with a balance of He.

^c Standard conditions were 40 Torr of CO and 100 Torr of O₂ and 620 Torr of He.

^d Standard conditions were 10 Torr C₆H₁₀ and 200 Torr of H₂ with a balance of He.

^e Normalized by the total number of surface atoms determined by ethylene hydrogenation.

^f The activity in this temperature regime displays “normal” Arrhenius temperature-dependent behavior; 170 °C–230 °C for CO oxidation, 130–160 °C for hydrogenation and 170–200 °C for dehydrogenation.

Pt/CeO₂ catalyst is more active and the reaction is less dependent on the oxygen concentration of the gas phase compared to Pt/ γ -Al₂O₃.

The OSC of CeO₂ depends on the ease of the reversible Ce⁴⁺/Ce³⁺ redox cycles, which can be affected by many factors, such as crystal facets, surface roughness, the concentration and distribution of oxygen vacancies, as well as the size of the oxygen vacancy clusters [36–38]. The predominant facets of the CeO₂ nanorods are crystallographically distinct from those of the nanooctahedra. These distinct differences in surface structure should be reflected in the catalytic properties of Pt/CeO₂ nanooctahedra and nanorods in the CO oxidation reaction. Indeed, the Pt/CeO₂ nanorods catalyst was found to be 17 times more active than Pt/CeO₂ nanooctahedra, with TOFs at 200 °C of 3.1 and 0.18 s⁻¹, respectively. The CeO₂ nanorods and nanooctahedra before Pt deposition show no CO conversion under the same reaction conditions. The activation energies for Pt/CeO₂ nanorods and nanooctahedra are 24.3 and 34.7 kcal/mol, respectively. These results are consistent with our XPS study, in which 60 and 28% of cerium exists as Ce³⁺ ions on the surface of CeO₂ nanorods and nanooctahedra, respectively. The high concentration of Ce³⁺ ions on the surface of the CeO₂ nanorods reflects the high concentration of surface oxygen vacancies. Because oxygen diffusion is considered to be the rate controlling step in the CO oxidation reaction on Pt/CeO₂ catalysts [36, 38], the high concentration of oxygen vacancies on CeO₂ nanorods enhances the

diffusion of oxygen, and thus, makes the Pt/CeO₂ nanorods more active compared with the Pt/CeO₂ nanooctahedra.

Cyclohexene hydrogenation-dehydrogenation over the Pt/CeO₂ catalysts was used as a model reaction to study the structural differences between the Pt species in the Pt/CeO₂ catalysts. Both hydrogenation and dehydrogenation products (cyclohexane and benzene respectively) are thermodynamically allowed and can be formed over Pt catalysts at the temperatures employed (120–200 °C). It has been demonstrated that the hydrogenation of cyclohexene to cyclohexane is structure insensitive, whereas the dehydrogenation of cyclohexene to benzene is structure sensitive [39–42]. The dehydrogenation of cyclohexene proceeds more rapidly on the Pt(100) crystal surface than on the Pt(111) crystal surface due to the different distributions of reaction intermediates on the Pt surfaces. The activity, TOF, and apparent activation energy for both the hydrogenation and dehydrogenation of cyclohexene are summarized in Table 1. As expected, the hydrogenation TOF at 120 °C was structure insensitive; the rates were around 10 s⁻¹ and the activation energies were around 10 kcal·mol⁻¹ for both catalysts. This result is in agreement with those for Pt single crystals reported previously. It also confirms that the numbers of available Pt sites determined by ethylene hydrogenation are correct. The kinetics of the dehydrogenation of cyclohexene at 150 °C are also reported in Table 1. The TOF values for dehydrogenation are 4.59 and 9.72 s⁻¹ for Pt/CeO₂ nanooctahedra and nanorods,

respectively. In other words, the selectivity to benzene over the Pt/CeO₂ nanorods is two times higher than that for the Pt/CeO₂ octahedra. The activation energies are 20.13 and 25.47 kcal·mol⁻¹ for Pt/CeO₂ nano-octahedra and nanorods, respectively. Similar structure-dependent selectivities and activation energies have also been observed in studies of Pt single crystals. [43, 44]. Under the same reaction conditions employed in this study, the selectivity to benzene on Pt(111) was higher than on Pt(100) and the activation energy for dehydrogenation on Pt(111) was lower than on Pt(100). Our results are not conclusive enough to determine the dominant crystal facets on the Pt nanocluster, but clearly indicate the structural differences between the epitaxial growth of Pt on CeO₂ nano-octahedra and the random growth of Pt on CeO₂ nanorods.

4. Conclusions

Pt nanocluster layers have been deposited on the surface of capping-agent-free CeO₂ nano-octahedra and nanorods via an e-beam evaporation strategy. The coverage of the Pt nanocluster layer could be controlled by adjusting the e-beam evaporation time. The e-beam evaporated Pt nanocluster layers on CeO₂ surfaces have a clean surface and a clean interface between Pt and CeO₂. Different growth behaviors of Pt on the two CeO₂ nanocrystals were observed. The epitaxial growth of Pt was observed on the CeO₂ octahedra. A high degree of lattice alignment between the Pt clusters on CeO₂ was shown in the HRTEM images of nano-octahedron system, but not in the nanorod system where the growth was random. The structures of the Pt clusters on the two different CeO₂ nanocrystals have been studied and compared by means of model reactions with the catalysts. The results of hydrogenation reactions clearly show the clean and similar chemical surface of Pt clusters in both catalysts. The support-dependent activity of these catalysts is demonstrated by CO oxidation. The Pt/CeO₂ nanorods show much higher activity compared with Pt/CeO₂ nano-octahedra because of the higher concentration of oxygen vacancies in the CeO₂ nanorods. The structure-dependent selectivity of dehydrogenation indicates that the structures of the Pt species on CeO₂

nanorods and nano-octahedra were different, showing how the metal deposition behavior can be modulated by the strong metal–metal oxide interactions.

Acknowledgements

This work was supported by Toyota Motor Engineering and Manufacturing North America (TEMA) Inc. We would like thank Dr. Kimber Stamm for helpful discussion.

Open Access: This article is distributed under the terms of the Creative Commons Attribution Noncommercial License which permits any noncommercial use, distribution, and reproduction in any medium, provided the original author(s) and source are credited.

References

- [1] Narayanan, R.; El-Sayed, M. A. Shape-dependent catalytic activity of platinum nanoparticles in colloidal solution. *Nano Lett.* **2004**, *4*, 1343–1348.
- [2] Zhang, Y.; Grass, M. E.; Habas, S. E.; Tao, F.; Zhang, T.; Yang, P.; Somorjai, G. A. One-step polyol synthesis and Langmuir–Blodgett monolayer formation of size-tunable monodisperse rhodium nanocrystals with catalytically active (111) surface structures. *J. Phys. Chem. C* **2007**, *111*, 12243–12253.
- [3] Huang, W.; Kuhn, J. N.; Tsung, C. K.; Zhang, Y.; Habas, S. E.; Yang, P.; Somorjai, G. A. Dendrimer templated synthesis of one nanometer Rh and Pt particles supported on mesoporous silica: Catalytic activity for ethylene and pyrrole hydrogenation. *Nano Lett* **2008**, *8*, 2027–2034.
- [4] Lim, B.; Jiang, M.; Camargo, P. H. C.; Cho, E. C.; Tao, J.; Lu, X.; Zhu, Y.; Xia, Y. Pd–Pt bimetallic nanodendrites with high activity for oxygen reduction. *Science* **2009**, *324*, 1302–1305.
- [5] Diebold, U. The surface science of titanium dioxide. *Surf. Sci. Rep.* **2003**, *48*, 53–229.
- [6] Haruta, M.; Date, M. Advances in the catalysis of Au nanoparticles. *Appl. Catal. A–Gen.* **2001**, *222*, 427–437.
- [7] Banares, M. A. Supported metal oxide and other catalysts for ethane conversion: A review. *Catal. Today* **1999**, *51*, 319–348.
- [8] Stakheev, A. Y.; Kustov, L. M. Effects of the support on the morphology and electronic properties of supported metal clusters: Modern concepts and progress in 1990s. *Appl. Catal. A–Gen.* **1999**, *188*, 3–35.



- [9] Bratlie, K. M.; Lee, H.; Komvopoulos, K.; Yang, P.; Somorjai, G. A. Platinum nanoparticle shape effects on benzene hydrogenation selectivity. *Nano Lett.* **2007**, *7*, 3097–4101.
- [10] Lee, H.; Habas, S. E.; Kveskin, S.; Butcher, D.; Somorjai, G. A.; Yang, P. Morphological control of catalytically active platinum nanocrystals. *Angew. Chem. Int. Ed.* **2006**, *45*, 7824–7828.
- [11] Peng, Z. M.; Yang, H. Paleostructural geomorphology of the Paleozoic central uplift belt and its constraint on the development of depositional facies in the Tarim Basin. *J. Am. Chem. Soc.* **2009**, *131*, 7542–7543.
- [12] Okumura, M.; Nakamura, S.; Tsubota, S.; Nakamura, T.; Azuma, M.; Haruta, M. Chemical vapor deposition of gold on Al₂O₃, SiO₂, and TiO₂ for the oxidation of CO and of H₂. *Catal. Lett.* **1998**, *51*, 53–58.
- [13] Kakuta, N.; Morishima, N.; Kotobuki, M.; Iwase, T.; Mizushima, T.; Sato, Y.; Matsuura, S. Oxygen storage capacity (OSC) of aged Pt/CeO₂/Al₂O₃ catalysts: Roles of Pt and CeO₂ supported on Al₂O₃. *Appl. Surf. Sci.* **1997**, *121/122*, 408–412.
- [14] Dutta, P.; Pal, S.; Seehra, M. S.; Shi, Y.; Eyring, E. M.; Ernst, R. D. Concentration of Ce³⁺ and oxygen vacancies in cerium oxide nanoparticles. *Chem. Mater.* **2006**, *18*, 5144–5146.
- [15] Schubert, M. M.; Plzak, V.; Garche, J.; Behm, R. CO oxidation over supported gold catalysts—“inert” and “active” support materials and their role for the oxygen supply during reaction. *J. Catal. Lett.* **2001**, *76*, 143–150.
- [16] Mai, H. X.; Sun, L. D.; Zhang, Y. W.; Si, R.; Feng, W.; Zhang, H. P.; Liu, H. C.; Yan, C. H. Shape-selective synthesis and oxygen storage behavior of ceria nanopolyhedra, nanorods, and nanocubes. *J. Phys. Chem. B* **2005**, *109*, 24380–24385.
- [17] Sun, C.; Sun, J.; Xiao, G.; Zhang, H.; Qiu, X.; Li, H.; Chen, L. Mesoscale organization of nearly monodisperse flowerlike ceria microspheres. *J. Phys. Chem. B* **2006**, *110*, 13445–13452.
- [18] Chen, G.; Xu, C.; Song, X.; Zhao, W.; Ding, Y.; Sun, S. Interface reaction route to two different kinds of CeO₂ nanotubes. *Inorg. Chem.* **2008**, *47*, 723–728.
- [19] Bernal, S.; Calvino, J. J.; Cauqui, M. A.; Gatica, J. M.; Larese, C.; Omil, J. A. P.; Pintado, J. M. Some recent results on metal/support interaction effects in NM/CeO₂ (NM: noble metal) catalysts. *Catal. Today* **1999**, *50*, 175–206.
- [20] Guzman, J.; Carretin, S.; Corma, A. Spectroscopic evidence for the supply of reactive oxygen during CO oxidation catalyzed by gold supported on nanocrystalline CeO₂. *J. Am. Chem. Soc.* **2005**, *127*, 3286–3287.
- [21] Huang, P. X.; Wu, F.; Zhu, B. L.; Gao, X. P.; Zhu, H. Y.; Yan, T. Y.; Huang, W. P.; Wu, S. H.; Song, D. Y. CeO₂ nanorods and gold nanocrystals supported on CeO₂ nanorods as catalyst. *J. Phys. Chem. B* **2005**, *109*, 19169–19174.
- [22] Hickey, N.; Larochette, P. A.; Gentilini, C.; Sordelli, L.; Olivi, L.; Polizzi, S.; Montini, T.; Fornasiero, P.; Pasquato, L.; Graziani, M. Monolayer protected gold nanoparticles on ceria for an efficient CO oxidation catalyst. *Chem. Mater.* **2007**, *19*, 650–651.
- [23] Wei, J. M.; Iglesia, E. Mechanism and site requirements for activation and chemical conversion of methane on supported Pt clusters and turnover rate comparisons among noble metals. *J. Phys. Chem. B* **2004**, *108*, 4094–4103.
- [24] Jacobs, G.; Graham, U. M.; Chenu, E.; Patterson, P. M.; Dozier, A.; Davis, B. H. Low-temperature water–gas shift: Impact of Pt promoter loading on the partial reduction of ceria and consequences for catalyst design. *J. Catal.* **2005**, *229*, 499–512.
- [25] Ferreira, A. P.; Zanchet, D.; Araujo, J. C. S.; Liberatori, J. W. C.; Souza-Aguiar, E. F.; Noronha, F. B.; Bueno, J. M. C. The effects of CeO₂ on the activity and stability of Pt supported catalysts for methane reforming, as addressed by *in situ* temperature resolved XAFS and TEM analysis. *J. Catal.* **2009**, *263*, 335–344.
- [26] Si, R.; Flytzani-Stephanopoulos, M. Shape and crystal-plane effects of nanoscale ceria on the activity of Au–CeO₂ catalysts for the water–gas shift reaction. *Angew. Chem. Int. Ed.* **2008**, *47*, 2884–2887.
- [27] Yan, L.; Yu, R.; Chen, J.; Xing, X. Template-free hydrothermal synthesis of CeO₂ nano-octahedrons and nanorods: Investigation of the morphology evolution. *Cryst. Growth Des.* **2008**, *8*, 1474–1477.
- [28] Schierbaum, K. D. Controlled synthesis of CeO₂ flower-like and well-aligned nanorod hierarchical architectures by a phosphate-assisted hydrothermal route. *Surf. Sci.* **1998**, *399*, 29–38.
- [29] Kotani, A.; Ogasawara, H. Theory of core-level spectroscopy of rare-earth oxides. *J. Electron Spectrosc. Rel. Phenom.* **1992**, *60*, 257–299.
- [30] Tsung, C. K.; Kuhn, J. N.; Huang, W. Y.; Aliaga, C.; Hung, L. I.; Somorjai, G. A.; Yang, P. D. Sub-10 nm platinum nanocrystals with size and shape control: Catalytic study for ethylene and pyrrole hydrogenation. *J. Am. Chem. Soc.* **2009**, *131*, 5816–5822.
- [31] Song, H.; Rioux, R. M.; Hoefelmeyer, J. D.; Komor, R.; Niesz, K.; Grass, M.; Yang, P. D.; Somorjai, G. A. Hydrothermal growth of mesoporous SBA-15 silica in the presence of PVP-stabilized Pt nanoparticles: Synthesis, characterization, and catalytic properties. *J. Am. Chem. Soc.*

- 2006, 128, 3027–3037.
- [32] Kuhn, J. N.; Tsung, C. K.; Huang, W.; Somorjai, G. A. Effect of organic capping layers over monodisperse platinum nanoparticles upon activity for ethylene hydrogenation and carbon monoxide oxidation. *J. Catal.* **2009**, 265, 209–215.
- [33] Trovarelli, A. Catalytic properties of ceria and CeO₂-containing materials. *Catal. Rev.-Sci. Eng.* **1996**, 38, 439–520.
- [34] Kaspar, J.; Fornasiero, P.; Hickey, N. Automotive catalytic converters: Current status and some perspectives. *Catal. Today* **2003**, 77, 419–449.
- [35] Oran, U.; Uner, D. Mechanisms of CO oxidation reaction and effect of chlorine ions on the CO oxidation reaction over Pt/CeO₂ and Pt/CeO₂/gamma-Al₂O₃ catalysts. *Appl. Catal. B-Environ.* **2004**, 54, 183–191.
- [36] Esch, F.; Fabris, S.; Zhou, L.; Montini, T.; Africh, C.; Fornasiero, P.; Comelli, G.; Rosei, R. Electron localization determines defect formation on ceria substrates. *Science* **2005**, 309, 752–755.
- [37] Sayle, T. X. T.; Parker, S. C.; Catlow, C. R. A. The role of oxygen vacancies on ceria surfaces in the oxidation of carbon monoxide. *Surf. Sci.* **1994**, 316, 329–336.
- [38] Liu, X. W.; Zhou, K. B.; Wang, L.; Wang, B. Y.; Li, Y. D. Oxygen vacancy clusters promoting reducibility and activity of ceria nanorods. *J. Am. Chem. Soc.* **2009**, 131, 3140–3141.
- [39] Segal, E.; Madon, R. J.; Boudart, M. The structure and activity of supported metal catalysts: I. Crystallite size and specific activity for benzene hydrogenation of platinum/silica catalysts. *J. Catal.* **1978**, 52, 45–49.
- [40] Dorling, T. A.; Moss, R. L. The structure and activity of supported metal catalysts: I. Crystallite size and specific activity for benzene hydrogenation of platinum/silica catalysts. *J. Catal.* **1966**, 5, 111–115.
- [41] Davis, S. M.; Somorjai, G. A. Correlation of cyclohexene reactions on platinum crystal surfaces over a ten-order-of-magnitude pressure range: Variations of structure sensitivity, rates, and reaction probabilities. *J. Catal.* **1980**, 65, 78–83.
- [42] McCrea, K. R.; Somorjai, G. A. SFG-surface vibrational spectroscopy studies of structure sensitivity and insensitivity in catalytic reactions: Cyclohexene dehydrogenation and ethylene hydrogenation on Pt(111) and Pt(100) crystal surfaces. *J. Mol. Catal. A-Chem.* **2000**, 163, 43–53.
- [43] Yang, M. C.; Rioux, R. M.; Somorjai, G. A. Reaction kinetics and *in situ* sum frequency generation surface vibrational spectroscopy studies of cycloalkene hydrogenation/dehydrogenation on Pt(111): Substituent effects and CO poisoning. *J. Catal.* **2006**, 237, 255–266.
- [44] Bratlie, K. M.; Flores, L. D.; Somorjai, G. A. Hydrogenation and dehydrogenation of cyclohexene on Pt(100): A sum frequency generation vibrational spectroscopic and kinetic study. *Surf. Sci.* **2005**, 599, 93–106.

